BEILSTEIN ARCHIVES

This open access document is published as a preprint in the Beilstein Archives with doi: 10.3762/bxiv.2019.126.v1 and is considered to be an early communication for feedback before peer review. Before citing this document, please check if a final, peer-reviewed version has been published in the Beilstein Journal of Nanotechnology.

This document is not formatted, has not undergone copyediting or typesetting, and may contain errors, unsubstantiated scientific claims or preliminary data.

Preprint Title	Construction of $NiMoO_4$ nanorods@ZIF-67 derived Co_3O_4 supported on cellulose based carbon aerogel for asymmetric supercapacitors
Authors	Meixia Wang, Jing Zhang, Xibin Yi, Benxue Liu, Xinfu Zhao and Xiaochan Liu
Publication Date	21 Okt 2019
Article Type	Full Research Paper
Supporting Information File 1	Supporting Information File 1.docx; 241.7 KB
ORCID® iDs	Jing Zhang - https://orcid.org/0000-0002-5257-6699

License and Terms: This document is copyright 2019 the Author(s); licensee Beilstein-Institut.

This is an open access publication under the terms of the Creative Commons Attribution License (http://creativecommons.org/licenses/by/4.0). Please note that the reuse, redistribution and reproduction in particular requires that the author(s) and source are credited.
The license is subject to the Beilstein Archives terms and conditions: https://www.beilstein-archives.org/xiv/terms.
The definitive version of this work can be found at: doi: https://doi.org/10.3762/bxiv.2019.126.v1

Construction of $NiMoO_4$ nanorods@ZIF-67 derived Co_3O_4 supported on cellulose based carbon aerogel for asymmetric supercapacitors

Meixia Wang, Jing Zhang*, Xibin Yi, Benxue Liu, Xinfu Zhao, Xiaochan Liu

Address: Shandong Key Laboratory for Special Silicon-containing Material, Advanced Materials Institute, Qilu University of Technology (Shandong Academy of Sciences), Jinan, 250014, P. R. China

Email: Jing Zhang - zhangjing@sdas.org

* Corresponding author

Abstract

In this study, $NiMoO_4$ nanorods @ ZIF-67 derived Co_3O_4 material supported by cellulose based carbon aerogel (CA) is successfully synthesized by two-step hydrothermal method. Benefitting from hierarchical porous structure, large specific surface and chemical composition, the $NiMoO_4$@Co_3O_4/CA ternary composite electrode delivers an enhanced specific capacitance of 1092.1 F/g at 0.5 A/g with the good rate capability (70.7% capacitance retention at 5.0 A/g). Besides, an advanced asymmetric supercapacitors (ASCs) is assembled by using the as-prepared $NiMoO_4$@Co_3O_4/CA ternary composite as a positive electrode and activated carbon (AC) as negative. The results suggest that the ASCs device exhibits a large capacitance of 125.4 F/g at 0.5 A/g, a highest energy density of 34.1 Wh/kg at a power density of 208.8 W/kg as well as cycling stability (84% after 2000 cycles), suggesting its great applications in energy storage. Namely, our results may provide a general approach to construct carbon aerogel and various MOF based composite

materials with hierarchical porous structure for potential applications in supercapacitor.

Keywords

Supercapacitors; Carbon aerogels; $NiMoO_4$; ZIF-67 derived Co_3O_4; Hierarchically porous structure

Introduction

Over recent years, the development of various new, renewable and clean energy conversion and storage devices has attracted wide attention worldwide attention in order to meet the worsening of environmental issue and energy demand [1-4]. Among them, supercapacitors have risen as promising candidates for energy storage owing to their fast charge/discharge property, high power density and long cycle life [5, 6]. Based on the charge storage mechanism, supercapacitors can be classified into the electrical double layer capacitor whose capacitance originates from electrostatic adsorption of reversible ions at the electrode/electrolyte interface and pseudocapacitors whose capacitance arises from reversible Faradaic reactions processes correlating with electro-active species [7, 8]. Compared with the electrical double layer capacitor, pseudocapacitors can provide a much higher specific capacitance owing to their rapid reversible redox reaction [9, 10]. Recently, advanced electrode materials based on various transition metal molybdates , such as $NiMoO_4$ [11], $CoMoO_4$ [12], $MnMoO_4$ [13] and $FeMoO_4$ [14], with the feasible oxidation states and unique electrochemical properties are regarded as one of the most promising materials for pseudocapacitors [15, 16]. Particularly, $NiMoO_4$ has been widely applied in high-performance pseudocapacitor, owing to its enhanced electrochemical

property generating from high electrochemical activity of the Ni ions and superb electrical conductivity of Mo ion [17-19]. Unfortunately, despite the fact that $NiMoO_4$ has high theoretical capacitance, it is still restricted by its low practical capacitance, poor rate performance and wettability for its widespread practical application in supercapacitor. Therefore, constructing an integrated hierarchical porous nanoarchitecture with a combination of two metal oxides materials is regarded as a brilliant way to greatly enhance the overall electrochemical performance, which is owing to their synergistic effects [20]. For example, Li et al. synthesized 3D hybrid $Co_3O_4/NiMoO_4$ nanowire/nanosheet arrays on carbon cloth, which exhibited a capacitance of 3.6 F/cm^2 at 3 mA/cm^2 and a capacitance retention of 82% with the increase of current density from 3 to 15 mA/cm^2 [21]. Cai et al. report a facile two-step hydrothermal method to synthesize the unique 3D $Co_3O_4/NiMoO_4$ core/shell nanowire arrays on Ni foam, and the resulting $Co_3O_4/NiMoO_4$ hybrid electrode exhibited areal capacitance of 5.7 F/cm^2 at a current density of 30 mA/cm^2 [22]. Zhang et al. described the fabrication of 3D hierarchical $Co_3O_4/NiMoO_4$ flower-like hybrid arrays on Ni foam with a high specific capacity of 636.8 C/g at a current density of 5 mA/cm^2 and capacitance retention of 84.1% after 2000 cycles [23]. Metal-organic frameworks (MOFs) with high porosity and tunable functionalities are ideal sacrificial templates to synthesize metal oxides [24-26]. As a result, Co_3O_4 derived from ZIF-67 is considered to be a rational electrode material as a MOFs derivative. It does not only maintain the original shape of MOF, but also has porous structure, which can compose graded porous structure with $NiMoO_4$. Consequently, such hierarchical porous nanoarchitecture can not only increase the specific surface area but also provide three-dimensional (3D) pathways for fast electrolyte ion diffusion and electron transport.

To date, Ni foam [27], copper grid [28] and titanium mesh [29] are mostly

selected as collectors, whereas the high cost of these materials limited the practical application. Carbon aerogel (CA) has been considered as an ideal supporting material to hybridize with electro-active materials because of their low cost, easy fabrication, large surface area, interconnected porosity and high electrical conductivity [30, 31]. Owing to its micro/mesoporous 3D morphology with large open pores could offer more space to grow electro-active materials, efficiently reduce internal resistance and enhance the rate capability. Therefore, a novel type of composites incorporating the electro-active metal oxides with hybrid nanorods and nanoparticles structure into a porous, conductive 3D networks of CA, could be promising electrode materials for supercapacitors.

Based on the above consideration, we present a facile and scalable strategy to fabricate integrated $NiMoO_4@Co_3O_4$ hierarchical porous structure aligned on CA derived from cellulose precursor for ASCs application. The $NiMoO_4$ nanorods uniformly grown on CA frameworks to support the loading of Co_3O_4 polyhedral nanocrystals originated from ZIF-67. The hierarchical porous structure of the as-prepared $NiMoO_4@Co_3O_4$/CA composite can provide adequate large space and reaction interface for shorting the ion diffusion length, and effectively buffering the volume change in the electrochemical reaction process. More importantly, such porous structure could enlarge the specific surface area, facilitate more active substances to participate in the reaction and improves its electrochemical performance. The results show that the as-synthesized $NiMoO_4@Co_3O_4$/CA//AC ASCs has relatively energy, power density and good cycle stability.

Results and Discussion

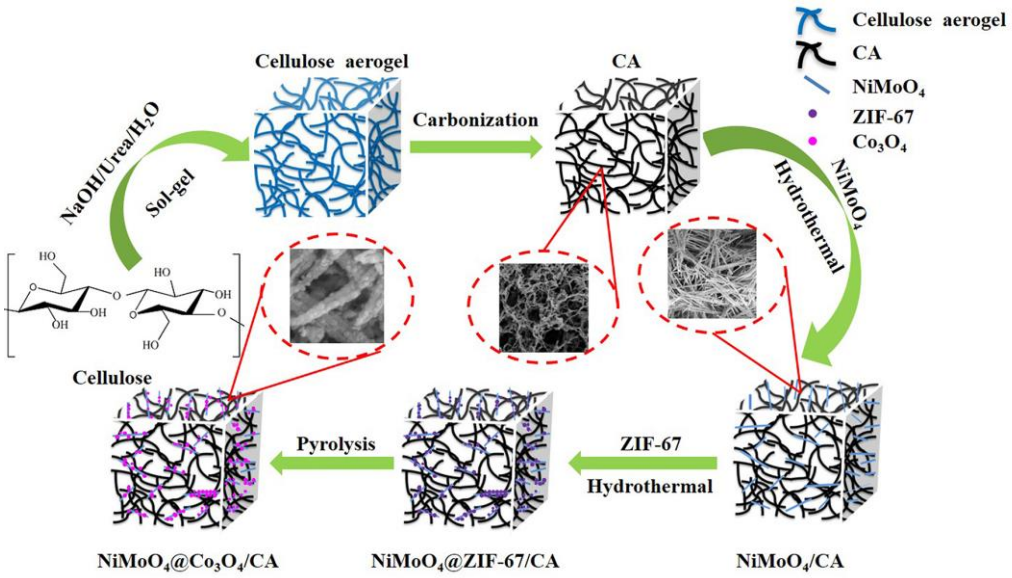

Fig. 1 The schematic illustration for the preparation of uniform hierarchical $NiMoO_4@Co_3O_4$/CA sample.

The synthetic procedure of $NiMoO_4@Co_3O_4$/CA composite as illustrated in Fig. 1. First, CA was obtained after undergoing the carbonization process of the cellulose aerogel precursor, which was produced from MC. Second, The CA described above can be used as the backbone for the growth of $NiMoO_4$ nanorods via hydrothermal method and the following heat treatment. The $NiMoO_4$/CA composite which uniformly filled $NiMoO_4$ nanorod into the 3D network of CA are obtained, which can provide plenty of sites for coupling with ZIF-67. Third, an in-situ crystallization of ZIF-67 on the surface of $NiMoO_4$/CA skeleton was carried out using hydrothermal method. Finally, after the pyrolysis of $NiMoO_4$@ZIF-67/CA precursors at 350 ℃ for 2 h under air atmosphere, the $NiMoO_4@Co_3O_4$/CA composite was obtained.

The morphologies and nanostructure of CA, $NiMoO_4$/CA, $NiMoO_4$@ZIF-67/CA and $NiMoO_4@Co_3O_4$/CA were investigated by SEM and TEM. As shown in Fig. S1 (Supporting Information), compared with the as-formed cellulose hydrogel and aerogel, the CA presented obvious volume shrinkage after the pyrolysis process.

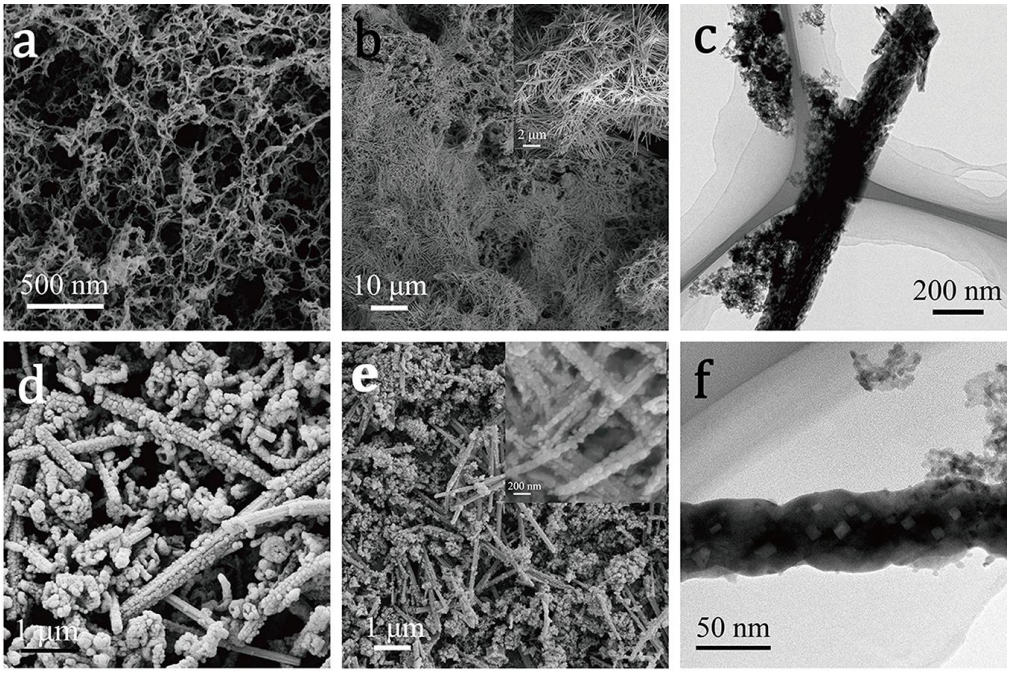

Fig. 2 (a) SEM image of CA; (b) SEM and (c) TEM images of $NiMoO_4$/CA; (d) SEM images of $NiMoO_4$@ZIF-67/CA; (e) SEM and (f) TEM images of $NiMoO_4$@Co_3O_4/CA.

Whereas, the nanofibrous network structures comprised of intertwined nanofibers of CA as shown in Fig. 2 (a) was still maintained from cellulose aerogel (Fig. S2, Supporting Information), and the diameter of the nanofibers is about 20~50 nm. The SEM top-view image of $NiMoO_4$ with homogenously distributing among interconnected nanofibers network of CA is showed in Fig. 2 (b). Meanwhile, from the SEM image with high magnification (inset of Fig. 2 (b)), each carbon nanofiber of CA is anchored around by plenty of nanorod-like $NiMoO_4$, which confirmed the CA are well hybridized with $NiMoO_4$ (Fig. 2 (c)). Such morphology is beneficial to be an ideal supporter for subsequent deposition of ZIF-67. The SEM images in Fig. 2 (d, e) show that ZIF-67 with the typical dodecahedral morphology have been uniformly grown on the surface of $NiMoO_4$ nanorods and also among the voids of $NiMoO_4$/CA composite. To transform the ZIF-67 into Co_3O_4 with annealing process as previously reported [32], the resultant Co_3O_4 exhibits a nest-like structure and porous morphology, yet the

dodecahedral structure can be largely kept with no apparent collapse. Besides, the TEM image in Fig. 2 (f) clearly shows that the Co_3O_4 particles are preferably grown on the surface of $NiMoO_4$ nanorods with a nest-like morphology. Such unique hierarchical porous architecture of $NiMoO_4$@Co_3O_4/CA is composed of three types of network structure: the first is a filamentous network with little bundling formed by interconnected nanofibers originating from CA, which could provide diffusion channels for electrolyte ions and also be a conductive substrate to serve as a backbone; the second consists of $NiMoO_4$ nanorods with interlaced growth, which plays a role of a bridge in the ternary hierarchical structure, can offer high surface area for large loading mass of active materials and also has a large contribution of pseudocapacitance value; the third is ZIF-67 derived Co_3O_4 nanoparticles, which has nanosized channels and cavities. The well-defined porous structure of nest-like Co_3O_4 is beneficial to provide more active sites for charge storage, improve the contact between electrode and electrolyte and facilitate the transport of electrons during the redox reactions [33]. It is clearly deduced that such a hierarchical structure can effectively enlarge specific surface area for Faradaic reactions, short diffusion pathways for the fast ion transfer, thus increase the supercapacitors performance.

The crystal structure of as-synthesized CA, $NiMoO_4$, ZIF-67 derived Co_3O_4, and $NiMoO_4$@Co_3O_4/CA was examined using XRD pattern as shown in Fig. 3 (a). For the CA, a broad diffraction peak at about 22.8° can be attributed to the (120) plane of amorphous carbon. The five well-defined diffraction peaks appearing at 2θ values of14.3, 25.3, 28.9, 33.7, and 53.9 ° could be indexed to the lattices of (110), (112), (220), (222), and (422) crystal planes of $NiMoO_4$, respectively, corresponding to that 14.3, 25.3, 28.9, 33.7, and 53.9 °could be indexed to the lattices could be indexed to the lattices of (110), (112), (220), (222), and (422) crystal planes of $NiMoO_4$, respectively, corresponding to that of the standard pattern (JCPDS No. 45-0142). In

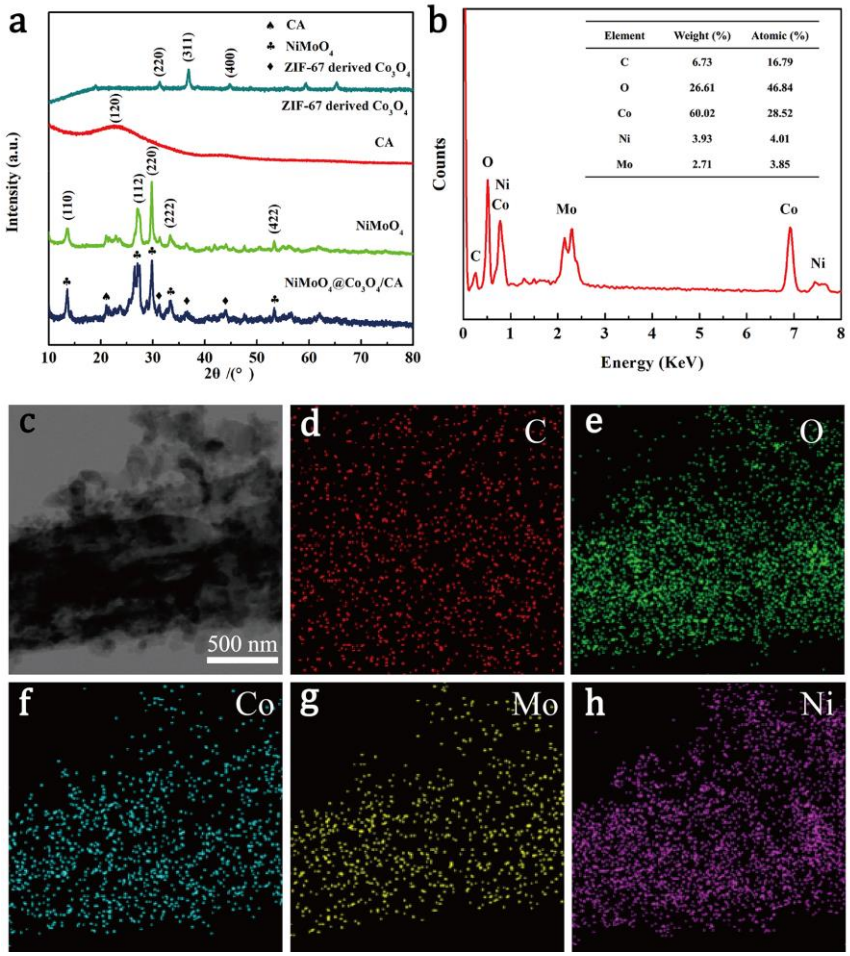

Fig. 3 (a) XRD patterns of ZIF-67 derived Co_3O_4, CA, $NiMoO_4$, $NiMoO_4$@Co_3O_4/CA; (b) EDS spectrum and (d-h) Elemental mapping of the as-prepared $NiMoO_4$@Co_3O_4/CA sample. The EDX patterns for elements of (d) C, (e) O, (f) Co, (g) Mo, and (h) Ni, respectively.

addition to the characteristic reflections from CA and $NiMoO_4$, ZIF-67 derived Co_3O_4 patterns were in good agreement with the standard patterns for Co_3O_4 (JCPDS No.42-1467). The intensity of diffraction peaks of CA and $NiMoO_4$ in the $NiMoO_4$@Co_3O_4/CA pattern was reduced due to the covering of ZIF-67 dodecahedron on the surface of the $NiMoO_4$/CA nanomaterial. To confirm the of $NiMoO_4$@Co_3O_4/CA heterostructure, energy dispersive spectrometer (EDS) spectrum and elemental mapping were carried out, as shown in Fig. 3 (b) and Fig. 3 (d-h). It can be clearly seen that there are signals for C, O, Co, Ni and Mo elements, indicating the coexistence of the Co_3O_4 phase and $NiMoO_4$ phase, which agrees well with the

results of XRD.

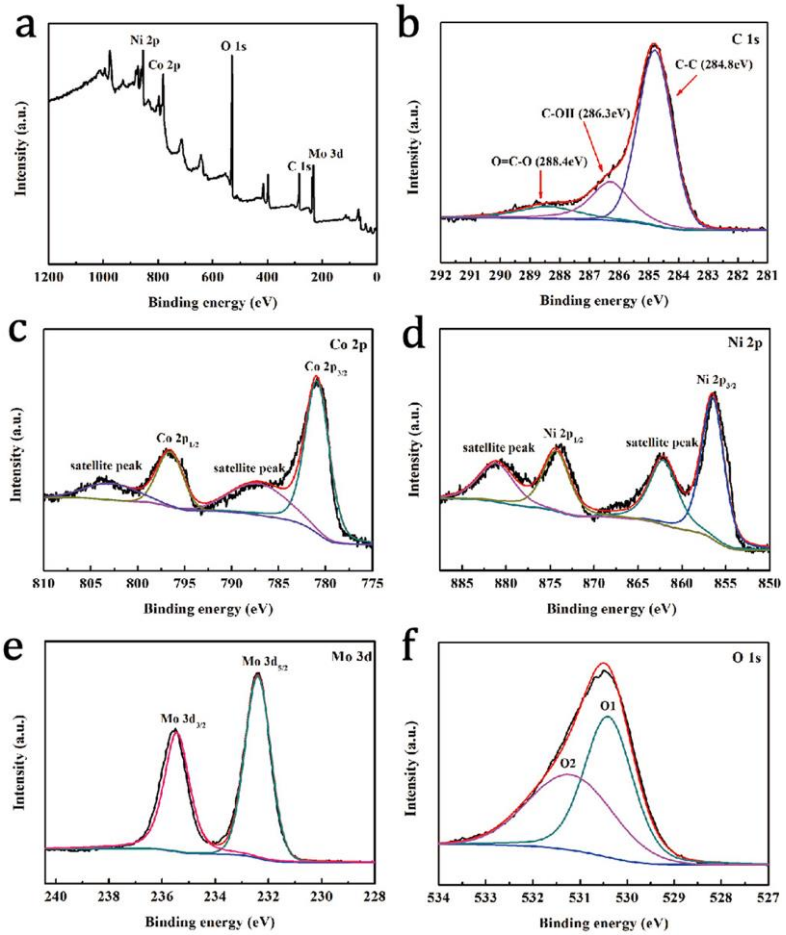

Fig. 4 XPS spectra of the NiMoO4@Co3O4/CA composite: (a) Survey spectrum; (b-f) Core-level spectra of (b) C1s, (c) Co 2p, (d) Ni 2p, (e) Mo 3d, and (f) O1s.

To investigate the chemical composition and valence states of the $NiMoO_4$@Co_3O_4/CA nanocomposite, XPS was performed and the results are shown in Fig. 4. According to Fig. 4 (a), the elements of Co, Ni, Mo, O and C can be clearly identified in the $NiMoO_4$@Co_3O_4/CA composites. The C 1s core-level XPS spectrum can be deconvoluted into three peaks, which corresponded to C-C (284.8 eV), C-OH (286.3 eV), and O=C-O (288.4 eV) bonds, respectively (Fig. 4 (b)) [34]. As depicted in Fig. 4 (c), two peaks are seen at 780.9 and 796.6 eV, corresponding to Co $2p_{3/2}$ and Co $2p_{1/2}$, respectively, indicating that the $NiMoO_4$@Co_3O_4/CA composite electrode material contains both Co^{3+} and Co^{2+} [35], whereas the peaks at 787.1 and

802.8 eV with a spin-energy separation of 15.7 eV can be attributed to the shake-up satellite peaks of Co^{2+} [36]. Fig. 4 (d) shows Ni 2p spectrum where two characteristic peaks at 856.5 and 874.3 eV and two shake-up satellite peaks with a spin-energy separation of 17.8 eV, corresponding to the Ni $2p_{3/2}$ and Ni $2p_{1/2}$ of Ni^{2+} [37, 38]. The Mo 3d core-level XPS spectrum (Fig. 4 (e)) showed two main peaks at 232.4 and 235.5 eV, corresponding to the Mo $3d_{5/2}$ and Mo $3d_{3/2}$ of Mo^{6+}, respectively [39]. Fig. 4 (f) shows the core-level XPS spectrum of O 1s. It can be divided into two main peaks with binding energies of 530.4 eV and 531.2 eV, which are attributed to typical metal oxygen bonds and surface low coordination oxygen ions, respectively [40]. The XPS results further indicated that the chemical composition of the as-synthesized $NiMoO_4@Co_3O_4$/CA sample contain C, Co, Ni, Mo and O elements.

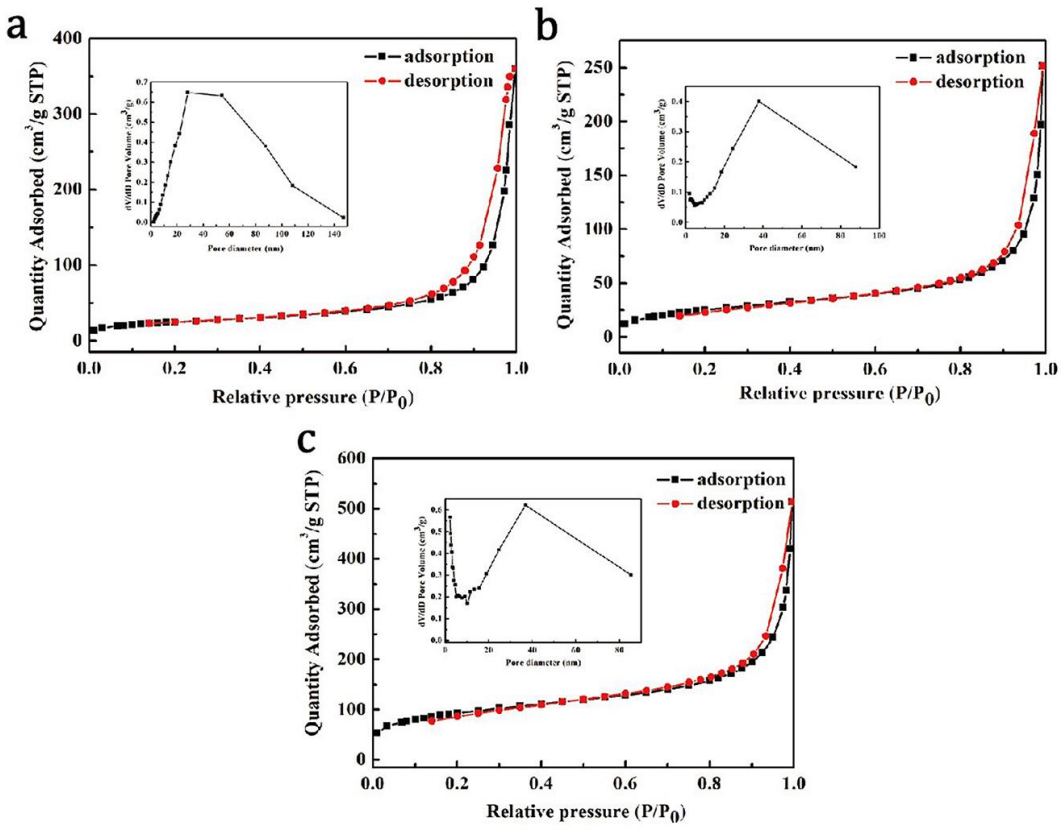

Fig. 5 Nitrogen adsorption/desorption isotherms and pore size distribution curves of (a) CA, (b) $NiMoO_4$/CA (b), and (c) $NiMoO_4@Co_3O_4$/CA composite.

The N_2 adsorption/desorption isotherms and pore size distributions of the CA, $NiMoO_4$/CA and $NiMoO_4$@Co_3O_4/CA samples are shown in Fig. 5, respectively. According to the IUPAC, both the CA and $NiMoO_4$/CA samples exhibit a typical type IV curves with distinct H_3-type hysteresis loops suggesting the existence of mesopores. Furthermore, the calculated BET specific surface area, total pore volumes and average diameters are listed in Table 1. From Fig. 5(c), it can be clearly seen that $NiMoO_4$@Co_3O_4/CA sample is a combination of Type IV and Type I isotherms, indicating the presence of micro and mesoporosity with monolayer-multilayer adsorption. Further, two distinct pore distributions are observed in the inset of Fig. 5(c), revealing the presence of hierarchically porosity: <5 nm micro/mesopores and 20-60 nm meso/macropores. As shown in Table 1, the $NiMoO_4$@Co_3O_4/CA sample has the largest S_{BET} of 334.47 m^2/g, and V_{total} of 0.8 cm^3/g, much higher than that of CA (87.7 m^2/g, 0.3 cm^3/g) and $NiMoO_4$/CA (94.9 m^2/g, 0.4 cm^3/g). The hierarchically porosity and large surface area of $NiMoO_4$@Co_3O_4/CA composite could be attributed to the aggregation and gathering of ZIF-67 dodecahedron grown on the porous skeleton of $NiMoO_4$/CA to form hierarchical porous structure, which is in agreement with the observation of the SEM image in Fig. 2. On the one hand, micropores mainly originates from ZIF-67 derived Co_3O_4, which can improve specific surface area and increase the active sites of charge storage. On the other hand, meso/macropores is consist of interconnected nanofibers originating from CA and interlaced $NiMoO_4$ nanorods, which can facilitate the soak of electrolytes into the particles and provide more open diffusion channels. Thus, it is easy to conclude that the obtained $NiMoO_4$@Co_3O_4/CA composite electrode can provide a new multi-functional platform for enhancing energy conversion and storage applications [41, 42].

Table 1: Pore structure parameters of the samples.

Sample	S_{BET}(m^2/g)	V_{total}(cm^3/g)	$D_{average}$(nm)
CA	87.66	0.31	24.34
$NiMoO_4$/CA	94.94	0. 40	14.95
$NiMoO_4$@Co_3O_4/CA	334.47	0.82	10.81

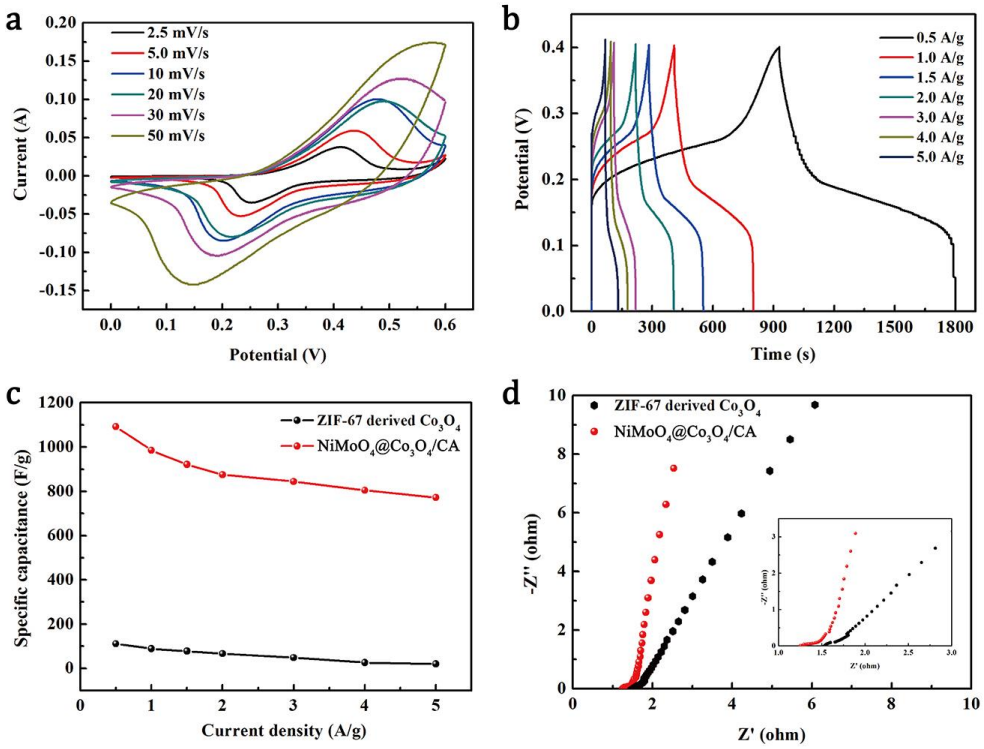

Fig. 6 (a) CV curves at various scan rate of 2.5~50 mV/s and (b) GCD curves at different current densities ranging from 0.5 to 5.0 A/g of the $NiMoO_4$@Co_3O_4/CA ternary composite. (c) Specific capacitance at various current densities and (d) EIS plots of pure ZIF-67 derived Co_3O_4 and $NiMoO_4$@Co_3O_4/CA electrodes.

Electrochemical measurements were performed to explore the potential application in supercapacitor. Fig. 6 (a) shows the CV curves of the $NiMoO_4$@Co_3O_4/CA electrode at voltage scan rates from 2.5 to 50 mV/s. Obviously, one pair of well-defined redox peaks can be observed in each the CV curve, which demonstrate that the capacitance arises mainly from the typical faradaic redox

reaction. To further evaluate the charge storage ability of the electrodes, GCD measurements were carried out within a potential window of 0 to 0.4 V at various current densities. As shown in Fig. 6 (b), the voltage plateau region appeared in all the GCD curves, meaning the faradaic pseudocapacitive behavior of the $NiMoO_4$@Co_3O_4/CA composite. Based on the GCD curves, the specific capacitance of the $NiMoO_4$@Co_3O_4/CA ternary composite is calculated to be 1092.1, 985.2, 921.3, 874.6, 844.5, 804.5 and 772.1 F/g at 0.5, 1.0, 2.0, 3.0, 4.0 and 5.0 A/g, respectively, which is far higher than that of pure ZIF-67 derived Co_3O_4 (111.4, 88.7, 78.2, 66.5, 48.7, 26.1 and 19.9 F/g at 0.5, 1.0, 2.0, 3.0, 4.0 and 5.0 A/g), clearly highlighting the advantages of the $NiMoO_4$@Co_3O_4/CA composite. At a high current density of 5.0 A/g, the specific capacitance of $NiMoO_4$@Co_3O_4/CA composite was still as high as 772.1 F/g, which is surpassing many metal oxides under the same conditions. The high capacitance of $NiMoO_4$@Co_3O_4/CA composite may be attributed to the following reasons. Firstly, CA can be used as an outstanding skeleton but also act as a conducting pathway in $NiMoO_4$@Co_3O_4/CA composite due to its excellent electrical conductivity and 3D carbon nano-network. Secondly, $NiMoO_4$ nanorods with extremely high pseudocapacitance is considered as an idealized deposition carrier for the nucleation and growth of ZIF-67 particles. Lastly, ZIF-67 derived Co_3O_4 possess a nest-like structure and porous morphology can offer high surface area, rich active sites and shorter diffusion path for the faradic effect reaction, which could result in higher capacitance.

In Fig. 6 (d), the $NiMoO_4$@Co_3O_4/CA composite shows higher phase angle than ZIF-67 derived Co_3O_4 in the low-frequency region, indicating that $NiMoO_4$@Co_3O_4/CA electrodes possess the lower diffusion impendence. After fitting the EIS plots based on the equivalent circuit model (inset of in Fig. 6 (d)), the solution resistance (R_s) value of $NiMoO_4$@Co_3O_4/CA composite is obtained to 1.3 Ω which is

smaller than that of ZIF-67 derived Co_3O_4 (1.5 Ω), demonstrating that the electrical conductivity is enhanced owing to the introduction of $NiMoO_4$/CA. The cycling stability of $NiMoO_4$@Co_3O_4/CA is tested over 2000 cycles at 0.5 A/g, the capacitance retention is up to 88.9% (Fig. S3, Supporting Information), which is very necessary and important for ASCs application.

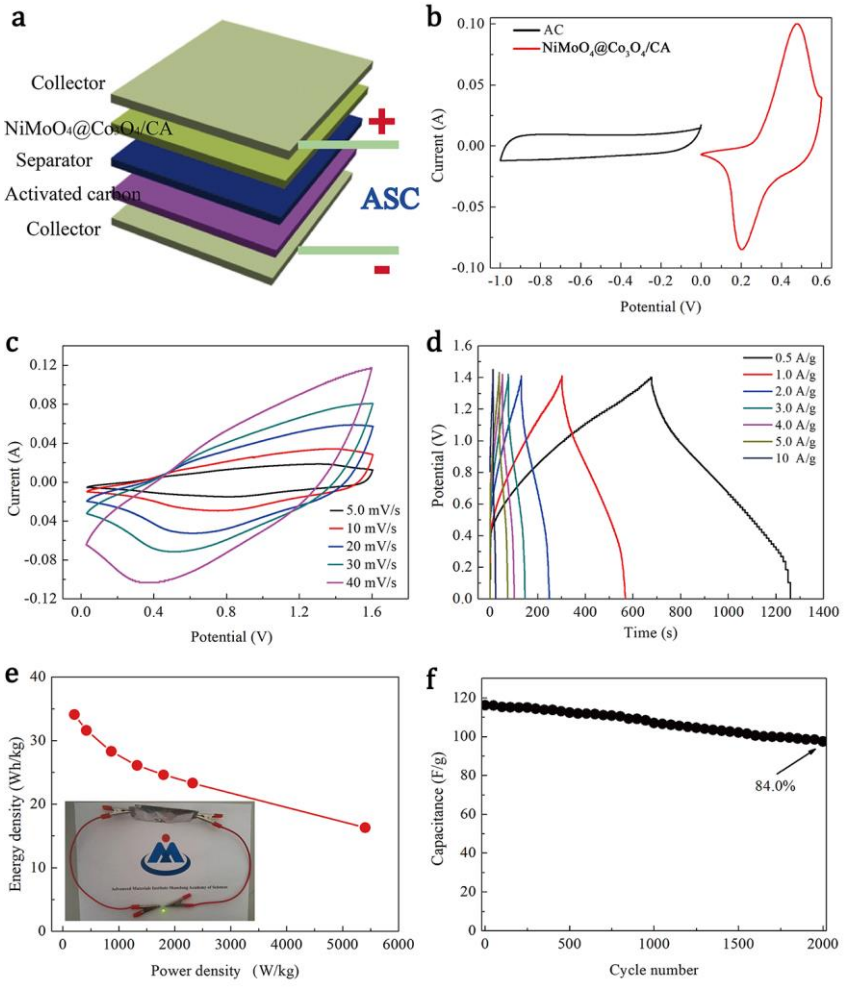

Fig. 7 Electrochemical performance of the $NiMoO_4$@Co_3O_4/CA//AC ASCs. (a) Schematic illustration of the as-fabricated ASCs device; (b) CV curves of the AC and $NiMoO_4$@Co_3O_4/CA electrodes with a scan rate of 5.0 mV/s; (c) CV curves at different scan rates; (d) GCD curves at different current densities; (e) Ragone plot related to energy and power densities; inset shows the green LED lighted up by assembled ASCs device; (f) Cycle performance of the ASCs device at current density of 0.5 A/g.

A schematic diagram of the ASCs device ($NiMoO_4@Co_3O_4$/CA//AC), which was fabricated by utilizing the as-prepared $NiMoO_4@Co_3O_4$/CA composite as the positive electrode and AC as the negative electrode, is shown in Fig. 7 (a). To determine the best working voltage window, the CV curves of the AC and $NiMoO_4@Co_3O_4$/CA electrodes at a scan rate of 5.0 mV/s are shown in Fig. 7 (b). It can be seen that the voltage window of AC is from -1.0 ~ 0 V and that of the $NiMoO_4@Co_3O_4$/CA is from 0 ~ 0.6 V with capacitive behaviors. Thus, the total voltage window of the ASCs device can reach 1.6 V, which is the sum of the voltage window for the AC and $NiMoO_4@Co_3O_4$/CA electrodes. Fig. 7 (c) exhibits the CV curves of the $NiMoO_4@Co_3O_4$/CA//AC ASCs at various scan rates from 2.5 to 50 mV/s. In Fig. 7 (c), we can clearly see that the overall capacitance of the $NiMoO_4@Co_3O_4$/CA//AC ASCs device originated from the combined contribution of Faradaic pseudocapacitance and EDLCs capacitance [43]. The shape of the CV curve displays the characteristics of hybrid ASCs, and there is no obvious distortion with the increase of scanning rate, which means a good capacitance behavior of the ASCs device. As demonstrated in Fig. 7 (d), the GCD curve was also evaluated to further discuss the rate performance of the ASCs device assembled up to 1.6 V. Based on the GCD curves, the specific capacity $NiMoO_4@Co_3O_4$/CA//AC ASCs device can reach 125.4 F/g at a current density of 0.5 A/g, and it still retains 59.8 F/g at a high current density of 10.0 A/g, indicating that the ASCs cell possesses good rate capability. The energy density and power density of the $NiMoO_4@Co_3O_4$/CA//AC ASCs are estimated to further confirm ASCs device electrochemical properties, and the Ragone plot between energy and power densities for the ASCs cell is shown in Fig. 7 (e). The energy density of $NiMoO_4@Co_3O_4$/CA//AC ASCs can increase from 16.3 to 34.1 Wh/kg as the power density decrease from 5403.3 to 208.8 W/kg. These values are significantly higher than the recently reported ASCs cell, such as

$NiCo_2O_4$@$NiMoO_4$ NMSAs//AC [44], Co_3O_4@$NiMoO_4$//AC [45]. Furthermore, the ASCs device shows the outstanding cycling performance at the current density of 0.5 A/g. As shown in Fig. 7 (f), the capacitance retention can keep 84.0% of the initial value after 2000 cycles. These results demonstrate that the $NiMoO_4$@Co_3O_4/CA//AC ASCs is very promising for practical application as a high-power energy device.

Conclusion

In summary, the hierarchical porous $NiMoO_4$@Co_3O_4/CA ternary composite has been successfully synthesized by a facile two-step hydrothermal method. The results $NiMoO_4$@Co_3O_4/CA electrode shows a largest specific capacitance as high as 1092.1 F/g at 0.5 A/g, and the synergy effect of three components is of great significance for outstanding electrochemical performance. The ASCs device based on the as-prepared $NiMoO_4$@Co_3O_4/CA and AC exhibits a large capacitance of 125.4 F/g at a current density of 0.5 A/g, a highest energy density of 34.1 Wh/kg at a power density of 208.8 W/kg, a maximum power density of 5405.3 W/kg at an energy density of 16.3 Wh/kg and excellent cycle stability with a capacitance retention of 84.0% of after 2000 cycles. The impressive enhancing performance of the ASCs device is attributed to the synergistic effect of 3D conductive porous structure derived from CA and the large specific capacitance contributed by transition metal oxides, suggesting that the $NiMoO_4$@Co_3O_4/CA ternary composite is quite promising as superior pseudocapacitive material for supercapacitor.

Experimental

2.1 Materials

Cobaltous nitrate hexahydrate ($Co(NO_3)_2 \cdot 6H_2O$), nickel nitrate hexahydrate ($Ni(NO_3)_2 \cdot 6H_2O$), sodium molybdat dihydrat ($Na_2MoO_4 \cdot 2H_2O$), 2-methylimidazole (2-MeIM), microcrystalline cellulose (MC, particle size: 50 μm) were purchased from

Aladdin Chemical Reagent Co. Ltd. Sodium hydroxide (NaOH), urea, methanol and anhydrous ethanol were purchased from Sinopharm Chemical Reagent Co. Ltd. Active carbon (AC) was purchased from Fujian Xinsen Carbon Industry Co. Ltd. All chemical reagents were analysis level, and they were all prepared without further processing. The deionized water was used in all experiments.

2.2 Synthesis of cellulose based carbon aerogel (CA)

Cellulose aerogel was produced from MC as follows: MC were immersed in 7% NaOH/12% urea aqueous solutions precooled at -12 ℃ in which the MC content was 5.0 wt%. Subsequently, the resulting mixture was under vigorous stirring for 20 min and then dripped into a small beaker at 75 ℃ for 6 h to form hydrogels before exchange in ethanol for 7 days, and subsequently such hydrogels were dried under supercritical CO2 to obtain cellulose aerogel. Finally, carbon aerogel (CA) was undergoing the carbonization process of the as-prepared cellulose aerogel at 800 ℃ for 2 h under N2 atmosphere with a heating rate of 2 ℃/min.

2.3 Preparation of NiMoO4/CA

The CA described above can be used as the backbone for the growth of NiMoO4 nanorods. Firstly, 4 mmol Ni(NO3)2·6H2O and 4 mmol Na2MoO4·2H2O were dissolved in 50 ml of deionized water to form a light-green solution and this process was kept at room temperature for 1 h to form homogeneous dispersion. The CA was soaked in the above solution and then transferred into 100 ml autoclave to keep under 150 ℃ for 6 h. After the reaction was completed, the yellow-black products were collected by filtration and washed with deionized water for several times.

Finally, the dried precipitates were annealed at 400 ℃ for 2 h under Air atmosphere to obtain the NiMoO4/CA samples.

2.4 Fabrication of $NiMoO_4$@ZIF-67 derived Co_3O_4/CA ($NiMoO_4$@Co_3O_4/CA) ternary composite

An in-situ crystallization of ZIF-67 on the surface of $NiMoO_4$/CA was carried out by the following process. Typically, 1 mmol $Co(NO_3)_2 \cdot 6H_2O$ and 4 mmol 2-MeIM were dissolved in 25 ml of methanol, respectively. The solutions above were mixed under vigorous stirring for 2 min. Then the solution and activated NiMoO4/CA were placed in a Teflon-lined autoclave. The autoclave was kept in 100 ℃ for 24 h and cooled to room temperature. The resulting ZIF-67/$NiMoO_4$/CA sample was washed by anhydrous ethanol, and then dried in vacuum at 80 ℃ for 12 h. Finally, $NiMoO_4$@Co_3O_4/CA sample was prepared by the pyrolysis of $NiMoO_4$@ZIF-67/CA precursors at 350 ℃ for 2 h under Air atmosphere.

2.5 Characterization

The crystalline structures of the prepared samples were characterized by X-ray powder diffraction (XRD, D8 Advance, Bruker) with Cu Kα radiation (λ=1540.6×10-4 nm) over a scan range of 5-80°. X-ray photoelectron spectroscopy (XPS, Thermo escalab 250Xi, Thermo fisher) measurements were performed using Al Kα monochromatized radiation at 1486.6 eV. The surface morphology of the samples was observed by scanning electron microscope (SEM, JSM-6701F, JEOL) at an accelerating voltage of 200 kV. Transmission electron microscopy (TEM) and energy dispersive X-ray spectroscopy (EDS) mapping investigations were analyzed using high resolution TEM (JEOL JEM-2100) operated at an acceleration voltage of 200 kV. The specific surface area determination and pore size analysis were recorded by

Brunauer-Emmett-Teller (BET) and Barrett-Joyner-Halenda (BJH) methods, respectively.

2.6 Electrochemical measurements

The electrochemical properties of $NiMoO_4@Co_3O_4$/CA electrodes were measured in a three-electrode testing system. Cyclic voltammetry (CV), galvanostatic charge/discharge (GCD) and electrochemistry impedance spectroscopy (EIS) were performed on the electrochemical workstation (CHI760D, Shanghai, China) in 2.0 M KOH aqueous solution. The working electrode materials were prepared by mixing the obtained sample, carbon black, acetylene black and polytetrafluoroethylene (PTEF) emulsion in a mass ratio of 80:7.5:7.5:5.0. The homogeneous slurry was coated on Ni foam substrates (1 cm × 1 cm) and dried at 80 ℃ for 12 h. The as-prepared electrodes loaded with the hybrid were then pressed at 5.0 MPa. The standard calomel electrode (SCE) and platinum electrode were used as the reference and counter electrodes respectively. The ASCs device was assembled used $NiMoO_4@Co_3O_4$/CA as the positive electrode, and AC as the negative. The details for preparation and characterization of ASCs are described in the Supporting Information. The cyclic stability tests are conducted on a LAND battery test system (LAND CT-2001A) at room temperature.

Supporting Information

Supporting Information File 1

Acknowledgements

This work is supported by the National Natural Science Foundation of China (21603125). Natural Science Foundation of Shandong Province (ZR2019BEM015,

ZR2019MEM034, ZR2019PB029), China Postdoctoral Science Foundation (2019M652452) and the Shandong's 2018 Support Plan for Innovative Talents.

References

1. Jiang, J.; Li, Y. Y.; Liu, J. P.; Huang, X. T.; Yuan, C. Z.; Lou, X. W. *Adv. Mater.*, **2012**, *24*, 5166-5180.

2. Martin W.; Brodd R. J. *Chem. Rev.*, **2004**, *104*, 4245-4270.

3. Yan, J.; Wang, Q.; Wei, T.; Fan, Z. J. *Adv. Energy Mater.*, **2014**, *4*, 1300816-1300859.

4. Yu, D. S.; Goh, K. L.; Wang, H.; Wei, L.; Jiang, W. C.; Zhang, Q.; Dai, L. M.; Chen, Y. *Nat. Nanotechnol.*, **2014**, *9*, 555-562.

5. Miller, J. R.; Simon, P. *Science,* **2008**, *321*, 651-652.

6. Kötz R.; Carlen, M. *Electrochim. Acta*, **2000**, *45*, 2483-2498.

7. Yu, Z.; Tetard, L.; Zhai, L.; Thomas, J. *Energy Environ. Sci.*, **2015**, *8*, 702-730.

8. Zhang, L. L.; Zhao, X. S.; *Chem. Soc. Rev.*, **2009**, *38*, 2520-2531.

9. Lei, Z. B.; Christov, N.; Zhao, X. S.; *Energy Environ. Sci.*, **2011**, *4*, 1866-1873.

10. Cao, X. H.; Shi, Y. M.; Shi, W. H.; Lu, G.; Huang, X.; Yan, Q. Y.; Zhang, Q.C.; Zhang, H. *Small*, **2011**, *7*, 3163-3168.

11. Cai, D. P.; Wang, D. D.; Liu, B.; Wang, Y. R.; Liu, Y.; Wang, L. L.; Li, H.; Huang, H.; Li Q. H.; Wang, T. H. *ACS Appl. Mater. Interfaces,* **2013**, *5*, 12905−12910.

12. Guo, D.; Zhang, H. M.; Yu, X. Z.; Zhang, M.; Zhang, P.; Li, Q .H.; Wang, T. H. *J. Mater. Chem. A*, **2013**, *1*, 7247-7254.

13. Cui, C. Y.; Xu, J. T.; Wang, L.; Guo, D.; Mao, M. L.; Ma, J. M.; Wang, T. H. *ACS Appl. Mater. Interfaces*, **2016**, *8*, 8568-8575.

14. Senthilkumar, B.; Selvan, R. K. *J. Colloid Interf. Sci.*, **2014**, *426*, 280-286.

15. Peng, S. J.; Li, L. L.; Wu, H. B.; Madhavi, S.; Lou, X. W. *Adv. Energy Mater.*, **2015**, *5*, 1401172-1401179.

16. Chen, T.; Shi, R.; Zhang, Y. Y.; Wang, Z. H. *ChemPlusChem*, **2019**, *6*, 69-77.

17. Liu, M. C.; Kong, L. B.; Lu, C.; Ma, X. J.; Li, X. M.; Luo Y. C.; Kang, L. *J. Mater. Chem. A*, **2013**, *1*, 1380-1387.

18. Haetge, J.; Djerdj, I.; Brezesinski, T. *Chem. Commun.*, **2012**, *48*, 6726-6728.

19. Huang, Y. P.; Cui, F.; Zhao, Y.; Lian, J. B.; Bao, J.; Liu T. X.; Li, H. M. *Inorg. Chem. Front.*, **2018**, *5*, 1594-1601.

20. Zhang, P.; Zhou, J. Y.; Chen, W. J.; Zhao, Y. Y.; Mu, X. M.; Zhang, Z. X.; Pan X. J.; Xie, E. Q. *Chem. Eng. J.*, **2017**, *307*, 687-695.

21. Li, Y. F.; Wang, H.; Jian, J. M.; Fan, Y.; Yu, L.; Cheng, G.; Zhou J. L.; Sun, M. *RSC Adv.*, **2016**, *6*, 13957-13963.

22. Cai, D. P.; Wang, D. D.; Liu, B.; Wang, L. L.; Liu, Y.; Li, H.; Wang, Y. R.; Li, Q.H.; Wang, T. H. *ACS Appl. Mater. Interfaces*, **2014**, *6*, 5050-5055.

23. Zhang, Y. R.; Yang, Y. F.; Mao, L. X.; Cheng, D.; Zhan, Z. Y.; Xiong, *J. Mater. Lett.*, **2016**, *182*, 298-301.

24. Wu, H. B.; Lou, X. W. *Sci. Adv.*, **2017**, *3*, 9252-9267.

25. Salunkhe, R. R.; Tang, J.; Kamachi, Y.; Nakato, T.; Kim J. H.; Yamauchi, Y. *ACS Nano*, **2015**, *9*, 6288-6296.

26. Zheng, S. S.; Li, X. R.; Yan, B. Y.; Hu, Q.; Xu, Y. X.; Xiao, X.; Xue H. G.; Pang, H. *Adv. Energy Mater.*, **2017**, *7*, 1602733-1602759.

27. Chen, S. M.; Zhang, Z. P.; Zeng, W. J.; Chen J. X.; Deng, L. B. *ChemElectroChem*, **2019**, *6*, 590-597.

28. Chen, H.; Zhou, M.; Wang, T.; Li F.; Zhang, Y. X. *J. Mater. Chem. A*, **2016**, *4*, 10786-10793.

29. Chen, H.; Yu, L.; Zhang J. M.; Liu, C. P. *Ceram. Int.*, **2016**, *42*, 18058-18063.

30. Zhuo, H.; Hu, Y. J.; Tong, X.; Zhong, L. X.; Peng X. W.; Sun, R. C. *Ind. Crop. Prod.*, **2016**, *87*, 229-235.

31. Guilminot, E.; Fischer, F.; Chatenet, M.; Rigacci, A.; Berthon-Fabry, S.; Achard P.; Chainet, E. *J. Power Sources*, **2007**, *166*, 104-111.

32. Chen, X. A.; Chen, X.; Zhang, F.; Zhi Y.; Huang, S. *J. Power Sources*, **2013**, *243*, 555-561.

33. Wang, M. X.; Zhang, J.; Fan, H. L.; Liu, B. X.; Yi, X. B.; Wang, J. Q. *New J. Chem.*, **2019**, *43*, 5666-5669.

34. Chen, L. B.; Bai, H.; Huang, Z. F.; Li, L. *Energy Environ. Sci.*, **2014**, *7*, 1750-1759.

35. Yang, X. J.; Sun, H. M.; Zan, P.; Zhao L. J.; Lian, J. S. *J. Mater. Chem. A*, **2016**, *4*, 18857-18867.

36. Li, J.; Lu, G. Z.; Wu, G. S.; Mao, D. S.; Guo, Y. L.; Wang Y. Q.; Guo, Y. *Catal. Sci. Technol.*, **2014**, *4*, 1268-1275.

37. Li, Y. F.; Jian, J. M.; Fan, Y.; Wang, H.; Yu, L.; Cheng, G.; Zhou J. L.; Sun, M. *RSC Adv.*, **2016**, *6*, 69627-69633.

38. Yan, J.; Fan, Z. J.; Sun, W.; Ning, G. Q.; Wei, T.; Zhang, Q.; Zhang, R. F.; Zhi L. J.; Wei, F. *Adv. Funct. Mater.*, **2012**, *22*, 2632-2641.

39. Chi, K.; Zhang, Z. Y.; Lv, Q. Y.; Xie, C. Y.; Xiao, J.; Xiao F.; Wang, S. *ACS Appl. Mater. Interfaces*, **2017**, *9*, 6044-6053.

40. Roginskaya, Y. E.; Morozova, O. V.; Lubnin, E. N.; Ulitina, Y. E.; Lopukhova G. V.; Trasatti, S. *Langmuir*, **1997**, *13*, 4621-4627.

41. Liu, J.; Yang, T.; Wang, D. W.; Lu, G. Q.; Zhao D.; Qiao, S. Z.; *Nat. Commun.*, **2013**, *42*, 798-805.

42. Xia, W.; Zou, R. Q.; An, L.; Xia D. G.; Guo, S. J. *Energy Environ. Sci.*, **2015**, *8*, 568-576.

43. Li, L.; Zhang, Y. Q.; Shi, F.; Zhang, Y. J.; Zhang, J. H.; Gu, C. D.; Wang X. L.; Tu, J. P. *ACS Appl. Mater. Interfaces*, **2014**, *6*, 18040-18047.

44 Zhang, C.; Xiao, J.; Lv, X. L.; Qian, L.H.; Yuan, S.L.; Wang S.; Lei, P. X. *J. Mater. Chem. A*, **2016**, *4*, 16516-16523.

45. Ma, X. J.; Kong, L. B.; Zhang, W. B.; Liu, M. C.; Luo Y. C.; Kang, L. *Electrochim. Acta*, **2014**, *130*, 660-669.